Rigid and differential plasma crystal rotation induced by magnetic fields

U. Konopka, D. Samsonov,* A. V. Ivlev,† J. Goree,* V. Steinberg,‡
and G. E. Morfill

Max-Planck-Institut für Extraterrestrische Physik, D-85740 Garching, Germany
(Received 14 June 1999)

Observations show that plasma crystals, suspended in the sheath of a radio-frequency discharge, rotate under the influence of a vertical magnetic field. Depending on the discharge conditions, two different cases are observed: a rigid-body rotation (all the particles move with a constant angular velocity) and sheared rotation (the angular velocity of particles has a radial distribution). When the discharge voltage is increased sufficiently, the particles may even reverse their direction of motion. A simple analytical model is used to explain qualitatively the mechanism of the observed particle motion and its dependence on the confining potential and discharge conditions. The model takes into account electrostatic, ion drag, neutral drag, and effective interparticle interaction forces. For the special case of rigid-body rotation, the confining potential is reconstructed. Using data for the radial dependence of particle rotation velocity, the shear stresses are estimated. The critical shear stress at which shear-induced melting occurs is used to roughly estimate the shear elastic modulus of the plasma crystal. The latter is also used to estimate the viscosity contribution due to elasticity in the plasma liquid. Further development is suggested in order to quantitatively implement these ideas.

PACS number(s): 52.25.Zb

I. INTRODUCTION

Micron-sized particles immersed in a plasma acquire a negative charge and may arrange themselves in ordered structures [1–6], which behave like a gas, liquid, or solid. This phenomenon, the ''plasma condensation,'' can be employed, e.g., in studying phase transitions [7–9] and low-frequency wave propagation [10–12]. In a typical dusty plasma experiment in a radio-frequency (rf) discharge, a thin single-layer or multilayer cloud of particles is levitated in the sheath at the lower electrode, where the electrostatic force due to the vertical electric field is strong enough to compensate for the weight of the particles. The particle cloud is shaped like a disk, suspended above the center of the electrode, and confined by a weak radial electric field. The collective processes in the particle cloud and its structural configuration are governed by interparticle coupling forces and by the ''external'' forces acting on the cloud, such as the ion drag, neutral friction, and electrostatic force due to the confining electric field [13,14]. In turn, all these forces, except the neutral friction, are functions of the single-particle potential. In general, the potential of each particle is assumed to be the screened Coulomb (Yukawa) potential, which is characterized by two parameters: the effective particle charge and the screening length. These parameters are assumed to be averaged over the rf-induced high-frequency variations. The usual methods to determine them are laser or electrical excitation of different types of low-frequency waves in the particle cloud [11,15–17] and, as shown recently, controlled collision of fast particles [18–20]. A new possible tool for the investigation of the forces acting on the particles is the study of the cloud in the presence of a magnetic field. Since the cloud is located in a region with a high electric field that has a radial component, adding a vertical magnetic field should result in an azimuthal $\mathbf{E}\times\mathbf{B}$ ion drift and therefore a rotation of the cloud in the horizontal plane. Particle cloud rotation due to this mechanism was observed in a dc glow discharge by Uchida *et al.* [21] and in a rf plasma by Law *et al.* [22]. Deflection of a single-particle trajectory was studied in an electron cyclotron resonance plasma by Nunomura *et al.* [23].

In the present paper we study the effect of a vertical magnetic field on the particle cloud in the sheath of an rf He plasma at various discharge conditions. All the parameters of the system are assumed to be the average of an rf period. We show that the magnetic-field results in a rotation of the cloud and that the angular velocity strongly depends on the plasma conditions, even changing its sign. We propose a simple analytical model describing the particle cloud motion, taking into account the electrostatic, ion drag, neutral drag, and interparticle interaction forces. One of the possible applications of plasma rotation, and oscillations induced by B, is to measure elastic and viscoelastic properties of the plasma condensed states. Order-of-magnitude estimates based on the data presented in this paper are given, and further directions in experiments are suggested.

II. EXPERIMENTAL SETUP

The experiments are performed in a gaseous electronics conference (GEC) rf reference cell [24] with a modified electrode system. Figure 1 shows the inner part of the apparatus. The powered lower electrode, surrounded by a ground shield, is capacitively coupled to an rf oscillator that generates a sinusoidal output voltage at a fixed frequency of 13.56 MHz. To introduce a magnetic field, a permanent magnet is installed under the lower electrode's surface. A ring-shaped upper electrode with an outer diameter of 130 mm and a thickness of 5 mm is at ground potential. A 40-mm-diam glass plate is installed in the central opening of the electrode.

─────────
*Present address: Department of Physics and Astronomy, The University of Iowa, Iowa City, IA 52242.

†Permanent address: High Energy Density Research Center RAS, 127412 Moscow, Russia.

‡Permanent address: Department of Physics of Complex Systems, Weizmann Institute of Science, Rehovot 76100, Israel.
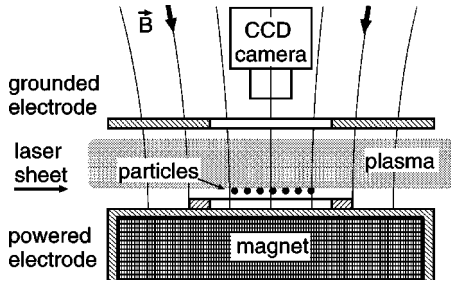
PRE <u>61</u>   1890

FIG. 1. Sketch of the inner part of the experimental setup.

The electrode separation is 30 mm. A digital oscilloscope is used to measure the peak-to-peak voltage as well as the negative self-bias at the driven electrode. Helium gas at a pressure $p = 0.2 - 3.0$ mbar is used for the discharge. The gas is not made to flow constantly (to avoid disturbances in particle motion during an experiment) but refilled at frequent intervals to prevent contamination.

We use melamine-formaldehyde spherical particles with a diameter of 8.9 ± 0.1 μm. They are introduced into the discharge through a 1-mm hole in the glass plate in the upper electrode. Since the distribution of the sphere diameters is narrow, the levitation height is equal for all particles until a first layer is filled. Only monolayer clouds are studied here. A 2-mm-thick copper ring with a 40-mm inner diameter is placed on the lower electrode. The ring enhances the radial component of the sheath electric field, which confines the particles in the center.

The particles are illuminated by a 30-mW He-Ne laser equipped with a cylindrical telescope to form a horizontal sheet of light of $\simeq 140$-μm thickness. The particles are imaged from the top by an external high speed (maximum 160 frames/s) digital charge-coupled-device (CCD) video camera with a 50-μm spatial resolution.

The cylindrical permanent magnet installed in the lower electrode produces a vertical magnetic field. The field lines point downward, and the field strength $B = 140 \pm 5\%$ G, measured by a Hall probe at the height of the suspended particles. Note that the presence of the plasma does not influence the magnetic field, since the typical value of the plasma magnetic susceptibility $|\chi_m| \sim n_e T_e / B^2 \sim 10^{-7}$ (where n_e and T_e are the electron density and temperature) is negligible.

The recorded video sequences are analyzed with a program that identifies individual particles and traces them from one frame to another. Having first determined the rotation center, we then calculate the angular velocity of each particle from the measured azimuthal displacement between consecutive frames and its distance from the rotation center, ρ. To reduce the uncertainties in the calculated values (due to pixel noise and limited camera resolution), the data are binned in radial 0.5-mm intervals and averaged in each bin. The uncertainties are then calculated as the standard deviation divided by the square root of the number of particles in the bin.

The electron temperature and density are measured at the center of the discharge with a rf-compensated passive Langmuir probe. The electron temperature T_e is found to be within 2.7–3.7 eV in all experiments, while the electron density n_e ranges from 5×10^8 cm^{-3} to 5×10^9 cm^{-3}.
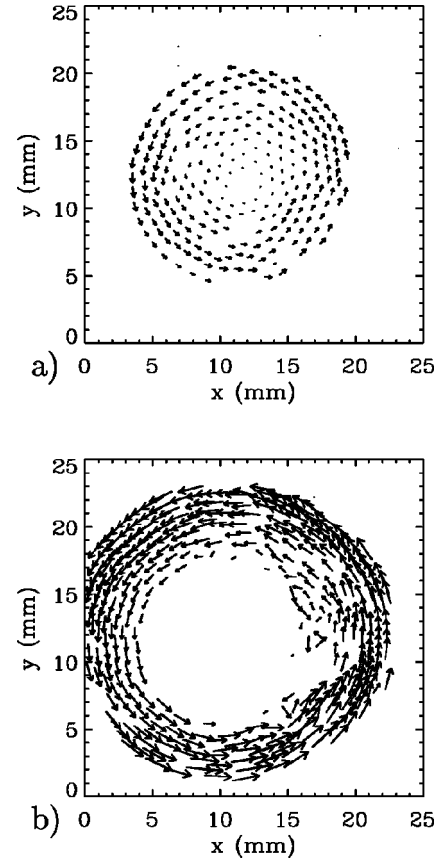

FIG. 2. Typical configuration of the particle cloud rotating in the magnetic field. The vectors indicate the particle displacement in 20 consecutive frames. The plots are made for two parameter sets (the discharge peak-to-peak rf voltage U_{PP}, the gas pressure p, the particle number N, and the frame rate): (a) $U_{PP} = 47$ V, $p = 0.40$ mbar, $N = 250 \pm 10\%$, 8 frames/s; (b) $U_{PP} = 82$ V, $p = 0.30$ mbar, $N = 450 \pm 10\%$, 6 frames/s.

III. EXPERIMENTAL RESULTS

Figure 2 shows a velocity map of a particle cloud rotating in the presence of the magnetic field. Individual particles move on almost circular trajectories. For low values of the discharge peak-to-peak rf voltage U_{PP}, the cloud is shaped like a disk with a small void in the center [Fig. 2(a)], whereas at high rf voltage the void diameter increases significantly and the cloud takes the form of a ring [Fig. 2(b)]. In all our experiments the particles form a monolayer.

The radial dependence of the particle angular velocity Ω is shown in Fig. 3 for three different rf voltages at varying gas pressure p. We keep the particle number N constant for each voltage. Figure 3(a) corresponds to the lower rf voltage. In this case the cloud rotates as a whole, practically without any shear motion. The angular velocity curves do not have significant radial dependence over the investigated gas pressure range. As the pressure increases (from curve 1 to 5) the rotation slows down. At higher rf voltage [Fig. 3(b)] the curves exhibit a strong radial dependence. As we increase the pressure (from curve 1 to 8) the angular velocity decreases and particles start rotating in the opposite direction. At even higher rf voltage [Fig. 3(c)] the angular velocity strongly changes between the center and the periphery.

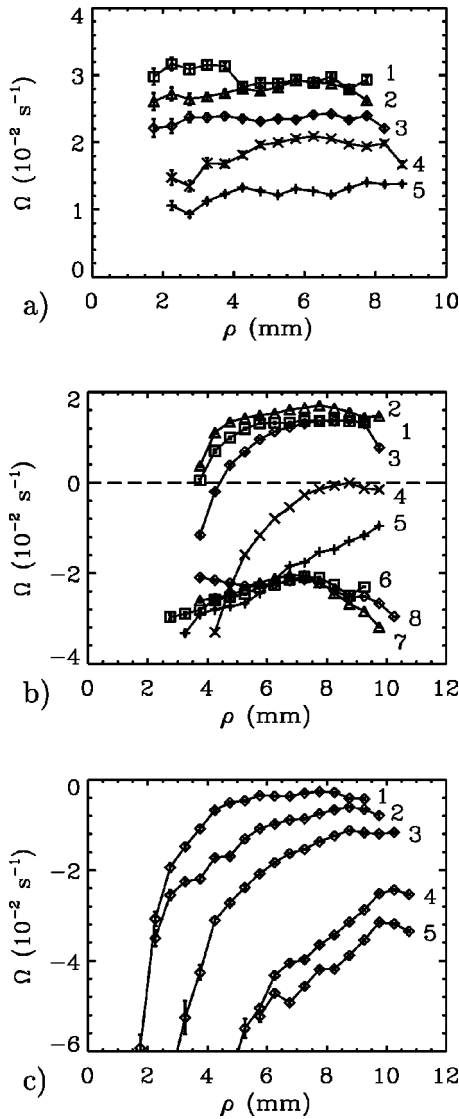Pair correlation functions $g(r)$ of the particles are shown

FIG. 3. Angular velocity Ω of the particles moving in the magnetic field vs distance ρ from the center of rotation. Positive values of the angular velocity correspond to counterclockwise rotation. Each figure shows a set of the curves taken at a fixed rf voltage U_{PP} and particle number N. Different curves correspond to different gas pressures p: (a) $U_{PP} = 47$ V, $N = 250 \pm 10\%$, and $p = 0.31$ mbar (1), 0.50 mbar (2), 0.60 mbar (3), 0.70 mbar (4), 0.80 mbar (5); (b) $U_{PP} = 82$ V, $N = 850 \pm 10\%$, and $p = 0.25$ mbar (1), 0.31 mbar (2), 0.49 mbar (3), 0.69 mbar (4), 0.80 mbar (5), 0.90 mbar (6), 1.08 mbar (7), 1.20 mbar (8); (c) $U_{PP} = 93$ V, $N = 700 \pm 10\%$, and $p = 0.41$ mbar (1), 0.61 mbar (2), 0.71 mbar (3), 0.90 mbar (4), 1.01 mbar (5).

in Figs. 4(a) and 4(b), corresponding to those in Figs. 3(a) and 3(c), respectively. The shape of $g(r)$ does not vary significantly with pressure for the same discharge voltage. We see that for small voltages [Fig. 4(a)] the phase state of the particles is more ordered and nearly crystalline, but as the voltage increases [Fig. 4(b)] it becomes liquidlike with only one peak in the correlation function. This last case corresponds to a strong shear due to differential rotation.

It was investigated whether the rotation depends on the size of the clouds for constant discharge conditions. Figure 5 shows the radial dependence of the angular velocity for different particle numbers in the cloud. It is obvious that, even
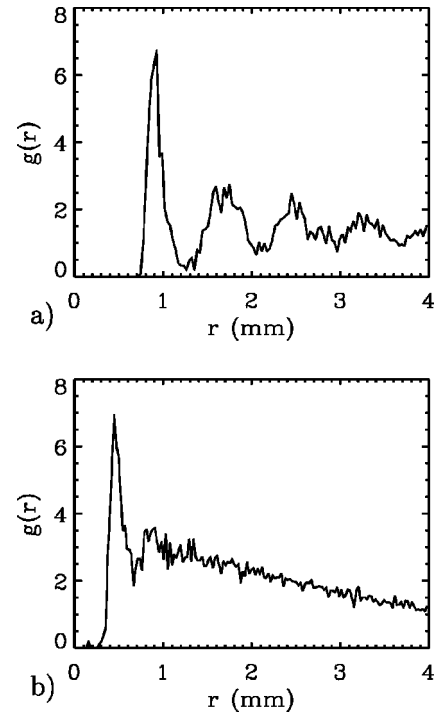

FIG. 4. The pair correlation functions $g(r)$ of the particle clouds. (a) and (b) correspond to the profiles of the angular velocity in Figs. 3(a) and 3(c), respectively.

though the size of the cloud increases significantly with the particle number (as shown on the inset), the angular velocity varies very little.

Another interesting observation illustrating a qualitative change in the confining potential (as discussed later) is shown in Fig. 6. Initially, particles form a large slowly rotating ring [Fig. 6(a)]. The rf voltage was increased suddenly, causing the particles to spiral toward the center [Fig. 6(b)] and the cloud to contract, forming a stable disk [Fig. 6(c)]. When the rf voltage is decreased, particles spiral outward, and the initial configuration is restored [Fig. 6(a)]. Both changes happen on a time scale of a few seconds.

IV. DISCUSSION

The experiments show that in the presence of a magnetic field the particle cloud is often shaped like a ring, in contrast
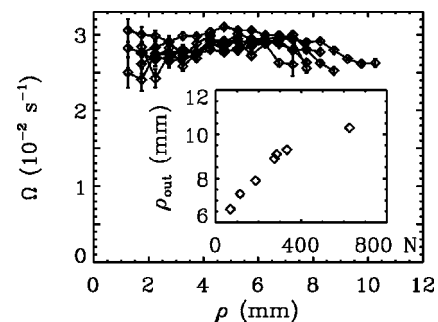

FIG. 5. Angular velocity Ω of the particles moving in the magnetic field vs distance ρ from the center of rotation. The curves are for 47-V rf peak-to-peak voltage and 0.5-mbar gas pressure. Different curves correspond to different particle numbers ranging from 60 to 620 particles in the cloud. The inset shows how the outer radius ρ_{out} of the cloud depends on the particle number N (the variance of the inner radius ρ_{in} is negligible).
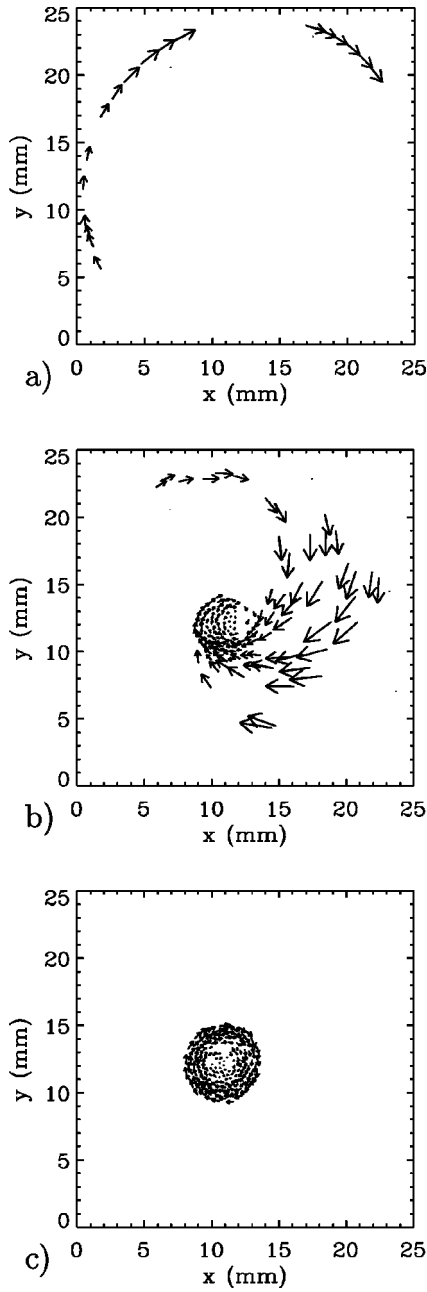
a)

b)

c)

FIG. 6. Three consecutive graphs showing the (a) initial, (b) intermediate, and (c) final stages of particle contraction to the center after suddenly increasing the rf peak-to-peak voltage on the electrodes from 100 V to 200 V, at 3-mbar gas pressure. The vectors indicate the particle displacement in 20 consecutive frames, the frame rate is (a) 20 frames/s and (b),(c) 30 frames/s. The contraction happens on the time scale of a few seconds. Decreasing the rf voltage restores the initial configuration (a).

to the case without the magnetic field at the same gas pressure and discharge voltage. In similar experiments with a magnetic coil (Ar discharge, $p \simeq 0.5$ mbar, $B \simeq 150$ G) it was observed by Law *et al.* [22] that after the magnetic field was switched on, the particles were swept away from the center and a void of $\simeq 5 - 6$ mm diameter was formed. Apparently, the magnetic field modifies the radial profile of the confining potential $\Phi_C(\rho) = -\int E_C(\rho) d\rho$ (where E_C is the weak confining electric field that results from both the ring shape of the confining electrode and ionization and magne-
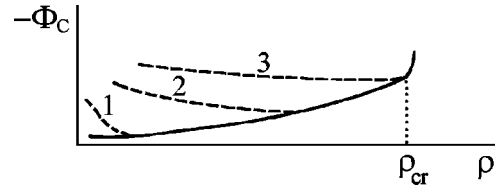

FIG. 7. Sketch of the qualitative change of the radial profile of the particle potential energy in a rf plasma with a vertical magnetic field. The curves (dashed lines) correspond to (1) low, (2) medium, and (3) high values of rf peak-to-peak voltage; $\rho = 0$ is the center of the electrode. The solid line shows the potential well in the absence of a magnetic field.

tization conditions of the plasma), and the maximum of the particle potential energy occurs in the center, as shown in Fig. 7. This effect is presumably due to the magnetization of the electrons: For $p \simeq 1$ mbar and at our magnetic-field strength, the ratio of the electron gyrofrequency to the frequency of the electron-neutral collisions exceeds unity, $\omega_{Be}/\nu_{en} \simeq 2$; for the ions, the ratio ω_{Bi}/ν_{in} is about 10^{-2}. Note also that numerical simulations of the electric potential in the discharge chamber using a two-dimensional fluid code from Boeuf and Pitchford [25] show that a small maximum of $-\Phi_C$ in the center can also arise in the absence of the magnetic field due to the perturbation caused by the glass plate in the upper electrode. However, for most of the discharge conditions used here the value of the radial electric field predicted by the simulation is insufficient to produce the void in the center of the cloud. The simulation also shows that starting from some critical radius $\rho \simeq \rho_{cr}$ (see Fig. 7) the radial electric field increases significantly. This is due to the sheath perturbation caused by the ring. Correspondingly, the profile of the confining potential $\Phi_C(\rho)$ becomes steep at the outer boundary. This effect is more significant at higher pressures.

We attribute the rotation of the cloud to the azimuthal component of the ion drag force F_{ID}^{ϕ} acting on the particles [23]. This component appears because of the azimuthal drift of the ions in crossed radial electric and vertical magnetic fields $\mathbf{E}_C \times \mathbf{B}$. The sign of F_{ID}^{ϕ} is determined by the sign of the confining field E_C. The shape of the potential $\Phi_C(\rho)$ strongly depends on the pressure and rf voltage, as explained above. For small values of U_{PP} the whole cloud rotates in a counterclockwise direction [Fig. 3(a)]. Thus, E_C must be positive (pointing radially outward) in the region occupied by the particles, except for maybe a small central part. The qualitative shape of the potential Φ_C in this case corresponds to curve 1 in Fig. 7. For the intermediate U_{PP}, the inner part of the cloud starts rotating in the opposite direction with an increase of pressure, which suggests that the profile of the potential resembles curve 2 [Fig. 3(b)]. At high U_{PP} the cloud rotates in a clockwise direction [Fig. 3(c)]. Therefore, E_C should be negative (radially pointing inward) nearly in the whole cloud, so that the shape of the potential should correspond to curve 3. In this case only a small number of particles at the outer boundary of the cloud ($\rho \simeq \rho_{cr}$) should continue to rotate in a counterclockwise direction. However, since the vertical electric field E_S at $\rho \simeq \rho_{cr}$ considerably exceeds that in the central part of the cloud, these particles

might well levitate above the laser sheet and become invisible.

Let us introduce cylindrical coordinates $\{\rho, \phi, z\}$, where the z axis is coincident with the vertical axis of symmetry and its origin is the electrode surface. In the vertical direction the equilibrium height z_{eq} of a particle is determined by the balance of the gravity force Mg, electrostatic force due to the sheath field $eZE_S(z_{eq})$, and the vertical projection of the ion drag force $F_{ID}^z(z_{eq})$. The particle mass in our experiments is $M \simeq 5.5 \times 10^{-10}$ g, so that the value of the electric field E_S at the equilibrium height can be estimated as 30 V/cm or more. Depending on the discharge conditions, z_{eq} varies from $\simeq 4.5$ mm to $\simeq 7$ mm. The steady circular motion of the particles in the horizontal plane is determined by the balance of the radial electrostatic force due to the confining electric field E_C, the radial and azimuthal components of the ion drag force $\mathbf{F}_{ID}$, the azimuthal friction force due to neutral-dust collisions F_{ND}^{ϕ}, and the force due to the coupling with the neighbor particles $\mathbf{F}_{NP}$ (the latter has both the radial and azimuthal components averaged over fluctuations and differs from zero in spatially nonuniform system, e.g., due to stresses). The resulting equation of motion for the particle is of the form

$$-M\Omega^2\rho\mathbf{n}_\rho = -eZE_C\mathbf{n}_\rho + \mathbf{F}_{ID}^{\perp} + F_{ND}^{\phi}\mathbf{n}_\phi + \mathbf{F}_{NP}, \qquad (1)$$

where Ω is the rotation angular velocity, $\mathbf{F}_{ID}^{\perp} = F_{ID}^\rho\mathbf{n}_\rho + F_{ID}^\phi\mathbf{n}_\phi$, $\mathbf{F}_{NP} = F_{NP}^\rho\mathbf{n}_\rho + F_{NP}^\phi\mathbf{n}_\phi$, and $\mathbf{n}_\rho$ and $\mathbf{n}_\phi$ are the unit vectors in the radial and azimuthal directions, respectively.

Using the equilibrium condition in the vertical direction, we obtain that the centrifugal force in Eq. (1) can be neglected when the following inequality is satisfied:

$$\frac{\Omega^2\rho}{g} \ll \frac{E_C}{E_S}.$$

The maximum value of the angular velocity in our experiments is about 5×10^{-2} s^{-1}, and the cloud radius $\rho \sim 1$ cm, so that the ratio of the centrifugal to the gravity acceleration does not exceed 10^{-6}. It follows from the results below that the ratio E_C/E_S is about $10^{-2} - 10^{-3}$. Thus, we can neglect the left-hand side of Eq. (1).

The neutral friction force (under the assumption of complete accommodation of the scattered He atoms) is given by expression [26]

$$F_{ND}^{\phi} = -\tfrac{4}{3}\delta m_n n_n v_{T_n}\pi a^2\Omega\rho, \qquad (2)$$

where a is the particle radius, m_n is the mass of He atom, $v_{T_n} = \sqrt{8T_n/\pi m_n}$ is the thermal velocity of the atoms, n_n is the gas atom number density, and $\delta \sim 1$ is a coefficient depending on the type of the atom scattering.

The ion drag force is determined by the ion drift velocity $\mathbf{u}$ of ions in the fields E_S, E_C, and B. For the pressure range $p \sim 0.1 - 1$ mbar the mean-free path of He$^+$ ions $l_i \sim 10^{-1} - 10^{-2}$ cm is of the order of or less than the vertical spatial scale of the sheath, and is much smaller than the radial scale of the confining potential in the region $\rho < \rho_{cr}$ (see Fig. 7). Consequently, for estimations at $\rho < \rho_{cr}$ the local relation be-

tween the velocity and the fields is valid. Using an empirical expression for the mobility of He$^+$ ions from Ref. [27], we get for the ion drift velocity

$$\mathbf{u} = \frac{(\mu_0/p)[\mathbf{E} + (\mathbf{u}/c)\times\mathbf{B}]}{\sqrt{1 + (\alpha_0/p)|\mathbf{E} + (\mathbf{u}/c)\times\mathbf{B}|}}, \qquad (3)$$

where the vectors $\mathbf{E}$ and $\mathbf{B}$ are

$$\mathbf{E} = E_C\mathbf{n}_\rho - E_S\mathbf{n}_z, \quad \mathbf{B} = -B\mathbf{n}_z$$

(the vector of the sheath electric field points down, $E_S > 0$), the ion mobility (at $p = 1$ mbar) $\mu_0 \simeq 12.2 \times 10^3$ mbar cm^2/V s, the coefficient $\alpha_0 \simeq 5.3 \times 10^{-2}$ mbar cm/V, and the pressure p is given in mbar units. Taking into account that $\mu_0 B/c \equiv \omega_{Bi}/\nu_{in} \ll 1$ and $|\mathbf{E} + (\mathbf{u}/c)\times\mathbf{B}| \simeq E_S$, we obtain from Eq. (3)

$$u_\rho = \frac{(\mu_0/p)E_C}{\sqrt{1 + (\alpha_0/p)E_S}},$$

$$u_\phi = \frac{1}{c}\frac{(\mu_0/p)^2 BE_C}{[1 + (\alpha_0/p)E_S]}, \qquad (4)$$

$$u_z = -\frac{(\mu_0/p)E_S}{\sqrt{1 + (\alpha_0/p)E_S}}.$$

Note that $|u_z| \gg |u_\rho| \gg |u_\phi|$. The ion drag force $\mathbf{F}_{ID}$ is a sum of two components—the collection and the orbit forces corresponding to the nonelastic and elastic collisions, respectively. Using expressions for both components derived in Ref. [13], we have

$$\mathbf{F}_{ID} = m_i n_i u_\Sigma \pi a^2(1 + \gamma\Delta + \gamma^2\Delta^2\Gamma)\mathbf{u}, \qquad (5)$$

where $m_i = m_n$ is the mass of He$^+$ ion, $v_{T_i} = \sqrt{8T_i/\pi m_i}$ is the thermal velocity of the ions, n_i is the ion density, $\gamma = e^2 Z/aT_e$ is a numerical factor depending on u_z and the ratio of the electron to ion temperature T_e/T_i (for our conditions, $\gamma \simeq 2 - 3$), Γ is the Coulomb logarithm for the ion-dust elastic collisions integrated over the interval from the ion collection impact parameter $b_c = a\sqrt{1 + \gamma\Delta}$ to the electron Debye length λ_{De},

$$\Gamma = \frac{1}{2}\ln\left(\frac{(\lambda_{De}/a)^2 + \gamma^2\Delta^2}{1 + \gamma\Delta + \gamma^2\Delta^2}\right).$$

If b_c exceeds λ_{De}, then the orbit force equals zero. The mean ion velocity u_Σ and the parameter Δ are

$$u_\Sigma \simeq \sqrt{v_{T_i}^2 + u_z^2}, \quad \Delta = \frac{\pi}{4}\frac{T_e}{T_i}\frac{v_{T_i}^2}{u_\Sigma^2}. \qquad (6)$$

Thus, Eq. (1) together with the expressions for the neutral friction force (2) and the ion drag force (5) describe the stationary circular motion of the particles in the cloud. Let us consider separately the forces acting in the radial and azimuthal directions.

In the radial direction the electrostatic force due to the confining electric field E_C is balanced by the radial component of the ion drag force F_{ID}^{ρ} (which is proportional to E_C and pointing opposite to the electrostatic force) and by the force due to the coupling with the neighbor particles F_{NP}^{ρ}

$$eZE_C = F_{ID}^{\rho} + F_{NP}^{\rho}.$$

When $|F_{ID}^{\rho}/E_C| < eZ$, the particles are located at the bottom of the potential well, where their potential energy is minimal (see Fig. 7). In the opposite case, when the ion drag force exceeds the electrostatic force, the particles should either contract in the central region or spread outward, depending on the shape of the potential $\Phi_C(\rho)$. Using Eqs. (4) and (5) we obtain the condition when the ion drag exceeds the electrostatic force

$$m_i n_i u_\Sigma \pi a^2 \frac{\mu_0}{eZp} \frac{(1 + \gamma\Delta + \gamma^2\Delta^2\Gamma)}{\sqrt{1 + (\alpha_0/p)E_S}} > 1. \tag{7}$$

For conditions typical for our experiments ($p \simeq 0.5$ mbar, $n_i \sim 10^9$ cm^{-3}, $T_e/T_i \sim 10^2$, $E_S \sim 30$ V/cm) the left-hand side of Eq. (7) is of the order of a few tenths. Thus, the particles should be located at the bottom of the potential well, which is consistent with the results of the observations. Using Eq. (6) for u_Σ and Δ and substituting in Eq. (5), we obtain the following dependence of the ion drag force on the pressure: $F_{ID}^{\rho}(p) \propto q(p)p^2$ for $p \lesssim \alpha_0 E_S \simeq 1 - 2$ mbar and $F_{ID}^{\rho}(p) \propto q(p)$ for $p \gtrsim \alpha_0 E_S$, where $q = n_i/n_n$ is the ionization fraction. The probe measurement data show that, for the conditions of our experiments, $q(p)$ decreases slightly with p. Therefore, raising the pressure up to a few mbar and increasing the rf voltage (and therefore the ion density) we can force the particles to contract to the center (see Fig. 6), because at high p and high U_{PP} the profile of the potential Φ_C should have the form of curve 3 in Fig. 7.

In the azimuthal direction, the corresponding component of the ion drag force is balanced by the neutral drag and the interparticle interaction forces

$$F_{ID}^{\phi} + F_{ND}^{\phi} + F_{NP}^{\phi} = 0.$$

In the case of a uniform particle distribution, F_{NP}^{ϕ} is averaged out to zero. Then the stationary rotation is determined by the balance of the total torques of the ion drag forces and the neutral friction forces. Thus, in the case of the uniform particle density, we obtain

$$\int_{\rho_{in}}^{\rho_{out}} (F_{ID}^{\phi} + F_{ND}^{\phi})\rho^2 d\rho = 0, \tag{8}$$

where ρ_{in} and ρ_{out} are the radii of the inner and outer boundaries of the cloud.

In some special cases the integral equation (8) can be reduced to the balance of the external forces F_{ID}^{ϕ} and F_{ND}^{ϕ}. For instance, it follows from Fig. 5 that for the used discharge conditions ($U_{PP} \simeq 47$ V, $p \simeq 0.5$ mbar) we have rigid-body cloud rotation, $\Omega(\rho) \simeq$ const. We see also that Ω is practically independent of the particle number N in the cloud, and therefore of ρ_{in} and ρ_{out}. Actually, only the outer radius ρ_{out} increases with N, because for the lower rf voltage

the potential well has the form of curve 1 in Fig. 7. Consequently, the integrand in Eq. (8) is close to zero for any ρ,

$$F_{ID}^{\phi} + F_{ND}^{\phi} \simeq 0. \tag{9}$$

Thus, for the discharge conditions corresponding to Fig. 5 the interparticle interaction force F_{NP}^{ϕ} is negligible.

Substituting the expressions for F_{ND}^{ϕ} and F_{ID}^{ϕ} from Eqs. (2) and (5) in Eq. (9) and using Eq. (4) we have

$$\frac{\mu_0^2 B E_C}{c\Omega\rho} \simeq \frac{4}{3}\delta \frac{v_{T_i}}{u_\Sigma}\frac{p^2}{q}\left(\frac{1 + (\alpha_0/p)E_S}{1 + \gamma\Delta + \gamma^2\Delta^2\Gamma}\right). \tag{10}$$

Equation (10) is the relation between the profile of the effective confining electric field $E_C(\rho)$ and the angular velocity Ω of the rigid-body rotation when F_{NP}^{ϕ} is negligible. The right-hand side of the relation is independent of the radius ρ (we assume that the vertical electric field of the sheath E_S is a constant). Therefore, within the accuracy of the experiment the confining electric field is directly proportional to ρ (for $\rho \gtrsim \rho_{in}$), i.e., the shape of the confining potential is close to a parabola, $-\Phi_C \propto \rho^2$. For Fig. 5, $\rho_{in} \simeq 1.5$ mm and the value of the electric field at $q \sim 10^{-7}$ is estimated as $E_C \sim 0.3\rho[$cm$]$ V/cm. Thus, for a cloud with a size of ~ 1 cm the ratio of the radial confining electric field to the vertical sheath field is of the order of $10^{-2} - 10^{-3}$. It follows also from Fig. 5 that the increase of the particle number in the cloud practically does not change the profile of the confining potential as well as the profile of the vertical electric field $E_S(z)$ (the equilibrium height z_{eq} does not depend on N either).

From our experimental data we can conclude that at $U_{PP} = 47$ V [see Fig. 3(a)] the confining potential remains close to parabolic up to $p \simeq 0.8$ mbar, so that $\Omega(\rho) \simeq$ const. Therefore, we can use Eqs. (6) and (10) to obtain the dependence of E_C on the pressure (for $p \lesssim 0.8$ mbar $< \alpha_0 E_S$): $E_C/\rho \propto \Omega(p)/\sqrt{p}q(p)$. Since Ω decreases with p and $q(p) \simeq$ const, the confining electric field also decreases with the pressure.

Thus, the parabolic confining potential always provides a rigid-body rotation with $\Omega =$ const, since for any $\rho_{in} \lesssim \rho \lesssim \rho_{out}$ the ion drag force $F_{ID}^{\phi} \propto \rho$ is balanced by the neutral friction force $F_{ND}^{\phi} \propto \rho$ and the interparticle interaction force vanishes. However, for the higher values of U_{PP} the confining potential changes, as shown in Fig. 7, and the angular velocity strongly changes from the center to the periphery. Therefore, F_{NP}^{ϕ} can become a crucial factor that determines the profile $\Omega(\rho)$. In order to solve a self-consistent problem of the particle cloud rotation in the nonparabolic confining potential, it is necessary to use some reasonable model describing the viscoelastic shear motion of the cloud in a liquid and crystalline states similar to what was developed for viscoelastic polymer solution flows [28]. The functional dependencies of the relaxation time and shear elasticity modulus on the particle coupling parameter can be obtained from the direct molecular-dynamic simulations for strongly coupled plasmas [29,30] or from simple plasma models [31]. The comparison of the results of the model with the experimental data on the cloud rotation will allow us to determine the particle coupling parameter and therefore give additional in-

formation about the single-particle potential in the cloud. This is the aim of our further investigations. However, we can use the data presented here to estimate these parameters to an order of magnitude.

V. SHEAR ELASTICITY, SHEAR-INDUCED MELTING, AND VISCOELASTICITY OF THE PLASMA CONDENSED STATES

Rotation of the plasma crystal in a magnetic field provides a possibility to measure elastic properties of the plasma crystal and viscosity of the plasma liquid, and to study structural transformations, plastic flow, dynamics of defects, and the melting transition under the shear stress. Part of these problems were studied both theoretically and experimentally in colloidal crystal [31–39], but there are at least two reasons to conduct these studies in the plasma condensed states. First, one can study in the plasma two-dimensional as well as three-dimensional structures. Second, one can compare equilibrium structures (colloidal crystal and liquid) with nonequilibrium structures (plasma condensed state).

The value of the elastic modulus of a plasma crystal can be estimated from the approximate relation $G \sim U n_p$, where n_p is the particle number density and U is the interparticle potential energy. Assuming that the potential of a single particle has the form of the Yukawa potential, we obtain

$$U(r) = \frac{Z^2 e^2}{r} \exp(-r/\lambda),$$

where Z is the effective particle charge and λ is the (electron) Debye screening length. In the case considered $d/\lambda \simeq 2$ (where the nearest-neighbor distance $d \simeq 0.06$ cm) one gets $U(d) \sim 10^2$ eV; that is, about one order of magnitude larger than the interaction energy between particles in the colloidal crystals and conventional solids. However, since the particle number density in the plasma crystals is much lower than in both former states and is of the order of $n_p \sim 10^4 - 10^5$ cm^{-3}, the characteristic value for the elastic modulus is $G \sim 10^{-5} - 10^{-6}$ dyn/cm^2. Thus, the plasma crystals show an extremely low value of the elastic modulus, about 5–6 orders less than even in colloidal crystals.

In the case considered it is very easy to reach extreme values of the ratio of the shear stress to the elastic constant in rather weak shear flows. Thus, even in a weak shear flow one can study not only the usual elastic response, but also highly nonlinear regimes, and shear-induced melting as well.

As shown above the magnetic field can play the role of a rather convenient parameter to induce and to control the shear rate. Two experimental methods can be employed to study the shear elastic properties of the plasma crystal and viscoelastic properties of the plasma liquid in the presence of an applied shear rate.

In the first method, which was used in the current experiment, a constant vertical magnetic field leads to a steady rotation of the particle cloud. Two different regimes of rotation were found in this experimental configuration and discussed above, namely, uniform (rigid-body) rotation with $\Omega(\rho) \simeq$ const in the case of the parabolic confined electrical potential $\Phi(\rho)$, and nonuniform rotation, when $\Phi(\rho)$ deviates from the parabolic shape. At $\Omega(\rho) \simeq$ const the shear
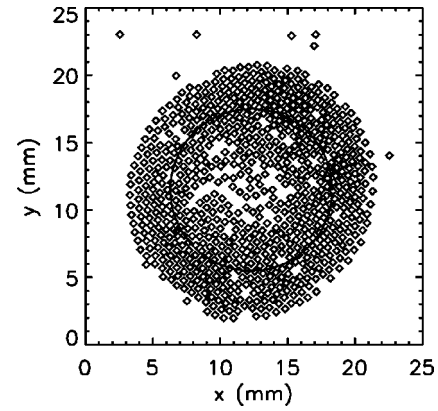

FIG. 8. Image of the particle distribution in the cloud corresponding to Fig. 3(b) with $p = 0.69$ mbar (curve 4). The solid circle separates an outer region with nearly solid-body rotation (ordered structure) and the inner region with differential rotation (liquidlike structure).

stress is negligible, and since two-dimensional flow is absolutely stable, the crystal symmetry will persist with increasing B until the highest Ω. Another way to vary Ω is to change the neutral gas pressure p as shown in Fig. 3. As follows from the data in Fig. 3(a), Ω increases about three times, while p decreases by the same ratio, and the crystal structure remains the same. On the other hand, the data presented [e.g., curves from 1 to 4 in Fig. 3(b)] show the region of $\Omega(\rho) \simeq$ const at large ρ together with the region of rather strong change of $\Omega(\rho)$ at smaller values of ρ.

In the outer region of $\Omega(\rho) \simeq$ const one finds the ordered crystal-like structure (see Fig. 8), while in the inner region, inside the solid circle in Fig. 8, the structure looks more disordered. It means that the crystal and liquid-like states coexist in this case. This is an example of the shear-induced melting.

Let us estimate the elastic shear modulus G_{sh} of the plasma crystal. For example, curve 4 [Fig. 3(b)] shows just one rotation direction and two well-defined regions of rigid and differential rotation. In the latter case the dependence $\Omega(\rho)$ can be approximated by $\Omega(\rho) \simeq 0.1(\rho[\text{cm}] - 0.7)$ s^{-1}. Then the average shear rate in this regime is $S = \langle \rho(d\Omega/d\rho) \rangle \simeq 5 \times 10^{-2}$ s^{-1}. Next, let us estimate the kinematic viscosity of He gas at $p = 0.7$ mbar. According to Epstein [26] one has $\eta = 0.35 m_n n_n v_{T_n} l_n$, where $l_n = (\sigma n_n)^{-1}$ is the mean-free path of He atoms. The cross section of He atom collisions is $\sigma \simeq 1.5 \times 10^{-15}$ cm^2, and correspondingly $l_n \simeq 0.03$ cm. Using this we find $\eta \simeq 1.6 \times 10^{-4}$ g/cm s. Assuming that the average shear stress ηS controls and causes the melting, and thus is equal to the plasma crystal shear modulus, one finds $G_{\text{sh}} = \eta S \simeq 8 \times 10^{-6}$ dyne/cm^2.

Using the three-dimensional model for the plasma crystal based on the Yukawa potential, one can relate the shear elastic modulus to the interparticle potential energy to estimate, e.g., the screening length. Indeed, in this case it was found [31] that $G_{\text{sh}} = (4/9)(d/\lambda)^2 n_p U(d)$, and one gets $\lambda \simeq 0.02$ cm. Of course, the model is three-dimensional, and estimates of n_p and $U(d)$ are rather crude, but one gets the correct estimates by the order of magnitude.

The second method to study shear elastic properties of a

particle cloud is to apply an oscillating magnetic field. This would lead to an oscillatory shear flow where both the frequency and the amplitude of B control the shear rate. Then the phase transformations, melting, and defect dynamics in a plastic flow could be studied as a function of the amplitude of the oscillating magnetic field. Similar methods with an oscillating shear flow have been developed for liquid crystals, colloids, a superfluid helium, etc., to study various properties. It was used, e.g., to measure the elastic shear modulus of the colloidal crystals with high resolution and accuracy [37,38].

Another possible application of shear flow due to the magnetic field is to measure the viscoelasticity of the colloidal liquid. Here one can expect not only the conventional contribution from the neutral gas viscosity and the hydrodynamic contribution of the particles (of the order of volume fraction), but also a contribution to the viscosity due to the interaction of the charged particles in the plasma liquid. The latter appears as a result of the elastic shear stresses in the fluid on a characteristic time smaller than that for a stress relaxation. As in the case of a colloidal liquid, one can make an order-of-magnitude estimate of this viscosity contribution η_1 and the characteristic stress relaxation time τ [38].The latter can be estimated from the Lindeman criterion: In a liquid a particle should oscillate with an amplitude exceeding the ''Lindeman distance'' of about $0.1d$. The characteristic relaxation time for conditions near the liquid-solid transition is the time of diffusion $\tau \simeq (0.1d)^2/D_0$, where $D_0 = kT/6\pi\eta a$ is the diffusion coefficient. Then the contribution to viscosity due to elasticity of colloidal liquid is $\eta_1 \simeq G_{\mathrm{sh}}\tau$. For the current experimental conditions we find $D_0 \simeq 3 \times 10^{-8}$ cm^2/s, $\tau \simeq 10^3$ s, and $\eta_1 \simeq 10^{-2}$ g/cm s. As one can see, $\eta_1 \gg \eta$, i.e., the plasma liquid is predicted to be extremely viscoelastic.

Finally, the characteristic stress relaxation time (which is, according to our estimates, rather large) can be measured from the shear-induced distortion of the pair correlation function $g(r)$ [33,35]. This method was introduced to define τ in the colloidal fluids, where the corresponding distortion of the static structure factor in the reciprocal space has been measured. In the plasma fluid the same idea can be applied by the direct optical measurements of the shear-induced distortion of $g(r)$ as a function of the shear rate.

VI. CONCLUSION

We have presented detailed observations of the rotation of a micron-sized particle monolayer (cloud) in the presence of a vertical magnetic field. The particles were suspended in the lower electrode sheath of a rf He discharge. We obtained the dependencies for the angular velocity of the particle motion on the distance from the vertical axis of symmetry for different conditions of the discharge by changing the rf peak-to-peak voltage and neutral gas pressure as well as the num-

ber of particles in the cloud. For low values of the rf voltage the angular velocity is practically independent of the distance (a rigid rotation), but for high voltage the angular velocity can vary significantly within the cloud, so that the inner part of the cloud, or even the whole cloud, changes its direction of rotation.

The cloud rotation is caused by the azimuthal component of the ion drag force acting on the particles, which is itself a result of the azimuthal ion drift in the crossed radial (confining) electric and vertical magnetic fields. We proposed a simple analytical model that takes into account the electrostatic, ion drag, neutral drag, and interparticle interaction forces and describes the stationary circular rotation of the particles in the cloud. Using this model, we have shown that for the rigid-body rotation the radial profile of the confining potential in the region of the cloud is nearly parabolic, and we estimated the value of the confining field. Based on our measurements we believe that for high values of the rf voltage the confining electric field is significantly modified by the magnetic field. Under some conditions the confining field changes sign near the discharge axis, causing the profile of the angular velocity to become strongly dependent on the distance from the rotation center. Thus the velocity field of the particles in the cloud can be considered as a measure of the confining electrical field, and the particles as local probes of this field.

We also demonstrated that experiments with particle clouds in the presence of a magnetic field open up the possibility to obtain the elastic and viscoelastic properties of strongly coupled colloidal plasmas, and as a result, the value of the particle coupling parameter. The data obtained in the present experiment already provide us information about the critical shear rate at which shear-induced melting of the plasma crystal occurs. It allows us to estimate the crystal shear modulus and therefore the particle potential energy of the interaction and the Debye screening length. We also estimated the viscosity contribution due to elasticity in the plasma liquid state. This estimate indicates that the plasma liquid state is expected to be extremely viscoelastic. The radial spatial particle distribution in the cloud gives information about the elastic modulus due to compression in the plasma condensed states. We discussed further methods to obtain quantitative information about the elastic moduli in two-dimensional plasma structures, the characteristic stress relaxation time, etc.

ACKNOWLEDGMENTS

[1] H. Thomas, G. E. Morfill, V. Demmel, J. Goree, B. Feuerbacher, and D. Möhlmann, Phys. Rev. Lett. **73**, 652 (1994).

[2] Y. Hayashi and K. Tachibana, Jpn. J. Appl. Phys., Part 2 **33**, L804 (1994).

[3] J. Chu and I. Lin, Physica A **205**, 183 (1994).

[4] J. Chu and I. Lin, Phys. Rev. Lett. **72**, 4009 (1994).

[5] A. Melzer, T. Trottenberg, and A. Piel, Phys. Lett. A **181**, 301 (1994).

[6] H. Thomas and G. Morfill, Nature (London) **379**, 806 (1996).

[7] J. Pieper, J. Goree, and R. Quinn, J. Vac. Sci. Technol. A **14**, 519 (1996).

[8] G. Morfill and H. Thomas, J. Vac. Sci. Technol. A **14**, 490 (1996).

[9] K. Tachibana and Y. Hayashi, Aust. J. Phys. **48**, 469 (1995).

[10] A. Melzer, A. Homann, and A. Piel, Phys. Rev. E **53**, 2757 (1996).

[11] M. Zuzic, H. M. Thomas, and G. E. Morfill, J. Vac. Sci. Technol. A **14**, 496 (1996).

[12] J. Pieper and J. Goree, Phys. Rev. Lett. **77**, 3137 (1996).

[13] M. S. Barnes, J. H. Keller, J. C. Forster, J. A. O'Neill, and D. K. Coultas, Phys. Rev. Lett. **68**, 313 (1992).

[14] T. Nitter, Plasma Sources Sci. Technol. **5**, 93 (1996).

[15] S. Peters, A. Homann, A. Melzer, and A. Piel, Phys. Lett. A **223**, 389 (1996).

[16] A. Homann, A. Melzer, S. Peters, and A. Piel, Phys. Rev. E **56**, 7138 (1997).

[17] A. Homann, A. Melzer, and A. Piel, Phys. Rev. E **59**, R3835 (1999).

[18] J. Konopka, L. Ratke, and H. M. Thomas, Phys. Rev. Lett. **79**, 1269 (1997).

[19] G. E. Morfill, H. Thomas, U. Konopka, and M. Zuzic, Phys. Plasmas **6**, 1769 (1999).

[20] U. Konopka, G. E. Morfill, and L. Ratke, Phys. Rev. Lett. (to be published).

[21] G. Uchida, R. Ozaki, S. Iizuka, and N. Sato, in *Proceedings of International Congress on Plasma Physics*, edited by P. Pavlo (European Physical Society, Prague, 1998), pp. 2557–2560.

[22] D. A. Law, W. H. Steel, E. B. Tomme, B. M. Annaratone, and J. E. Allen (unpublished).

[23] S. Nunomura, N. Ohno, and S. Takamura, Jpn. J. Appl. Phys., Part 1, **36**, 877 (1997).

[24] P. J. Hargis, Jr., K. E. Greenberg, P. A. Miller, J. B. Gerardo, J. R. Torczynski, M. E. Riley, G. A. Hebner, J. R. Roberts, J. K. Olthoff, J. R. Whetstone, R. J. van Brunt, M. A. Sobolewski, H. M. Anderson, M. P. Splichal, J. L. Mock, P. Bletzinger, A. Garscadden, R. A. Gottscho, G. Selwyn, M. Dalvie, J. E. Heidenreich, J. W. Butterbaugh, M. L. Brake, M. L. Passow, J. Pender, A. Lujan, M. E. Elta, D. B. Graves, H. H. Sawin, M. J. Kushner, J. T. Verdeyen, R. Horwath, and T. R. Turner, Rev. Sci. Instrum. **65**, 140 (1994).

[25] J. Boeuf and L. C. Pitchford, Phys. Rev. E **51**, 1376 (1995).

[26] P. S. Epstein, Phys. Rev. **23**, 710 (1924).

[27] L. S. Frost, Phys. Rev. **105**, 354 (1957).

[28] R. B. Bird, Ch. Curtiss, R. C. Armstrong, and O. Hassager, *Dynamics of Polymeric Liquids* (Wiley, New York, 1987), Vols. 1 and 2.

[29] B. Bernu and P. Vieillefosse, Phys. Rev. A **18**, 2345 (1978).

[30] W. L. Slattery, G. D. Doolen, and H. E. DeWitt, Phys. Rev. A **21**, 2087 (1980).

[31] J. F. Joanny, J. Colloid Interface Sci. **71**, 622 (1979).

[32] P. Pieranski, Contemp. Phys. **24**, 25 (1983).

[33] N. A. Clark and B. J. Ackerson, Phys. Rev. Lett. **44**, 1005 (1980).

[34] B. J. Ackerson and N. A. Clark, Phys. Rev. Lett. **46**, 123 (1981).

[35] B. J. Ackerson and N. A. Clark, Physica A **118**, 221 (1983).

[36] B. J. Ackerson and N. A. Clark, Phys. Rev. A **30**, 906 (1984).

[37] H. M. Lindsay and P. M. Chaikin, J. Chem. Phys. **76**, 3774 (1982).

[38] H. M. Lindsay and P. M. Chaikin, J. Phys. (Paris), Colloq. **46**, C3-269 (1985).

[39] D. A. Weitz, W. D. Dozier, and P. M. Chaikin, J. Phys. (Paris), Colloq. **46**, C3-257 (1985).